
Article:
Benakis, M., Costanzo, D. and Patran, A. (2020) Current mode effects on weld bead geometry and heat affected zone in pulsed wire arc additive manufacturing of Ti-6-4 and Inconel 718. Journal of Manufacturing Processes, 60. pp. 61-74. ISSN: 1526-6125

https://doi.org/10.1016/j.jmapro.2020.10.018

Current mode effects on weld bead geometry and heat affected zone in Pulsed Wire Arc Additive Manufacturing of Ti-6-4 and Inconel 718

Michalis Benakis[1,2*], Davide Costanzo[1] and Alin Patran[2]

[1] *Department of Physics and Astronomy, University of Sheffield, Sheffield, S3 7RH, UK*
[2] *Advanced Remanufacturing and Technology Centre (ARTC), 637143, Singapore*

*Corresponding author
E-mail address: m.benakis@sheffield.ac.uk (M. Benakis).

Abstract

For the last decade, additive manufacturing (AM) has been revolutionising the aerospace industry, building and repairing various components for aircrafts and outer space vehicles. Despite the fact that AM is gaining rapid adoption by the industry, it is still considered a developing technology, with ongoing research in a variety of fields. Wire arc additive manufacturing (WAAM), a welding-based AM technology, is an active field of research as well, because it enables economical production of large-scale metal components with relatively high deposition rates. In this article, the effects on the weld-bead geometry and heat affected zone from high and low frequency pulsed current are explored on Gas Tungsten Arc Welding (GTAW). The materials used in this investigation were selected to be Ti-6-4 and Inconel 718, both highly used in the aerospace industry for their high strength-to-weight ratio and strength at elevated temperatures respectively. The design of the experiments followed a Taguchi-inspired orthogonal array, altering, apart from the current modes and values, the torch travel speed driven by an industrial robotic arm as well as the wire-feeding rate.

The results demonstrate the ability to control both the weld-bead dimensions and penetration depth, as well as the heat affected regions, by utilizing the dual pulsing combination of both high and low frequency pulsing. Alterations from wide beads with deep penetration to narrower beads with greater height-to-width ratios are demonstrated in a single manufacturing setup, enabling further development of the WAAM process.

Keywords: *Wire Arc Additive Manufacturing; Pulsed-GTAW; Additive manufacturing; Welding input parameters; Weld bead geometry.*

1 Introduction

Additive manufacturing (AM), also known as 3D-printing and rapid prototyping, refers to the fabrication of objects from three-dimensional model data by adding materials in a layer-upon-layer manner [1,2]. This manufacturing approach is currently experiencing a high popularity, being regarded as one of the most studied processes in recent times [3]. The reason behind this popularity lies in the benefits of AM, mainly the ability to create complex shapes and product designs that were previously prohibited by conventional means of traditional manufacturing (casting, subtractive manufacturing, etc.), reduced time to market from design to final product and the higher utilization of material compared to the traditional manufacturing processes. As a result, AM is attractive to industrial sectors that utilize expensive materials e.g. titanium alloys, superalloys (nickel-based alloys), such as aerospace, energy, medicine and defense [4]. Additionally, the freedom to explore more complex designs results in replacing compound structures with a single complex component, reducing weight and allowing fabrication of structures with lower buy-to-fly ratios.

Examples of AM applied in aerospace have been seen in both aircraft and spacecraft propulsion systems (e.g. aircraft titanium fuel nozzles, rocket engine regenerative-cooled nozzles, the pogo accumulator) and structural assemblies (e.g. Airbus A350 titanium brackets, waveguide brackets on NASA's JUNO spacecraft). AM is also expected to have widespread application in the aerospace maintenance, repair and overhaul industry (MRO), providing product repairs with a reduced remanufacturing cost of 50% compared to conventional manufacturing [5].

Mainly originating from welding technologies, there are different metal AM processes, each with its own advantages and disadvantages, making them suitable for specific applications. The AM processes are classified either by the form of the material feeding technology used, or by their heat source. Processes where the additive material is in the form of powder in a container with the heat applied directly on top of it are called "powder bed" technologies, where the processes with powder delivered into the melt pool generated by the heat source are called "blown powder" technologies. Processes where the additive material is provided in the form of a wire are termed "wire fed" technologies. When classified by heat source used for the material melting, there are three main metal AM categories: electron beam based, laser based and electric arc based.

1.1 Wire Arc Additive Manufacturing

The process combining the wire feeding technology with an electric arc power source is usually called wire arc additive manufacturing (WAAM). Other names include welding shape deposition, 3D welding, shape metal deposition (SMD), shape welding and structural weld build-up [6]. WAAM uses an arc welding power source to melt the wire-shaped additive material which is guided by a motion platform

and a digital control platform. Apart from its simplicity compared to other AM methods, WAAM provides a variety of other benefits. In particular it has the ability to manufacture large components, as opposed to powder bed and electron beam based AM methods where the manufacturing dimensions are restricted by the powder bed size and the vacuum chamber respectively [7]. This allows the manufacturing of larger aerospace frame components like wing spars resulting in additional cost savings both in weight and production time. Another benefit of the process is the minimal waste of feedstock compared to blown powder methods. The ability of the system to control the wire feed-rate and direct it to the weld pool provides high material consumption efficiency. WAAM has also the ability to deliver higher deposition rates compared to other AM processes [8]. Additional benefits of WAAM include the relatively low cost of equipment, high power efficiency (40%–90%) and larger selection of materials since welding is a more mature process than AM [9–11].

WAAM can be performed using three main types of welding technologies. The most frequently used is metal inert gas (MIG), also known as gas metal arc welding (GMAW). The main benefit of MIG is that the wire, which is also the consumable electrode that forms the arc, is positioned coaxially to the welding torch, which allows higher freedom of movement in contrast with the non-consumable electrode methods like tungsten inert gas (TIG) and plasma arc welding (PAW) where the filler wire is added sideways between the electrode and the workpiece. A modified MIG variant named cold metal transfer (CMT) based on controlled dip transfer mode has been reported to provide weld beads of high quality and low thermal heat on aluminium and steel [12]. When applied to titanium, the process is unfortunately experiencing arc wandering resulting in increased surface roughness. Therefore TIG and PAW are the processes of choice for WAAM of titanium alloys [13].

TIG, also known as gas tungsten arc welding (GTAW), is a welding process where the welding arc is formed between a non-consumable tungsten electrode and the workpiece, with the filler material added from the side. Since the electrode is non-consumable, greater control over the electrode-workpiece distance can be achieved, resulting in greater arc stability than in processes with consumable electrodes. Additionally, GTAW can produce cleaner welds of greater finish than MIG, due to reduced spatter, as metal droplet transfer is better controlled. GTAW however, requires more time to complete a weld than MIG, as it is a slower process [14]. The GTAW process can operate on both direct and alternating current depending of the application.

1.2 Pulsed-GTAW

Pulsed-GTAW, is an advanced welding technology where the welding current undergoes modulation, switching between high and low preset values during regular intervals (pulses) [15,16]. As a result of

this technology greater control of the heat input is achieved, with subsequent regulation of the weld pool behavior and solidification.

When the pulse frequency is low (1-10 Hz), thermal pulsing is occurring, enabling joining of materials with different thermal conductivity or dissimilar geometries, as well as difficult joints in thin materials. During the thermal pulse duration, the material is melting a single spot until the melt pool reaches the desired penetration. The current is then switched to the lower value, reducing the heat and allowing solidification to occur, while simultaneously providing sufficient energy to maintain the arc. The cycle is then repeated to the next point along the welding path, resulting in a series of overlapping identical single-spot welds [17]. By avoiding the excessive heat built up that would have been accumulated with DC current mode, the thermal pulsing provides lower heat input and subsequently reduced Heat Affected Zone (HAZ), while delivering the desired weld properties with uniformly penetration depth [18–20].

High frequency pulsing currents (>1 kHz), also referred to as InterPulse, have the ability to agitate the molten pool via forces generated as a result of the high frequency [18]. An arc root radius reduction witnessed in welding with high frequency current is resulting in narrower weld beads [21]. Studies on correlation between the arc root radius and the pulsing frequency have shown that with increasing frequencies the plasma root radius decreases [22,23]. Additionally, with high frequency pulsed currents the arc force is significantly increased as the frequency increases [24]. This results in greater axial pressure, causing more depression of the weld pool surface and achieving increased weld penetration [22]. Higher energy density is also achieved, narrowing the HAZ and allowing higher welding speeds to be applied. Additionally, the arc stiffness is increased resulting in less arc wander [25,26].

1.3 Desired bead geometry in WAAM

WAAM is considered a near net shape (NNS) process, meaning that the fabricated parts are close to their final geometries while still requiring further processing (e.g. machining, surface finishing) to reach their final form. In order to reach closer to net shape, a higher printing resolution is required; the results vary from process to process. To achieve the level of printing accuracy in WAAM, proper control over penetration depth, weld cap reinforcement and bead width is required (Figure 1). Built-up passes may significantly differ from the root pass, where deep penetration with wide bead width is desired for a robust structural foundation. These demands require interchanging modes of operation in the same environment, provided either by different equipment or by a setup that can provide a variety of bead geometries.

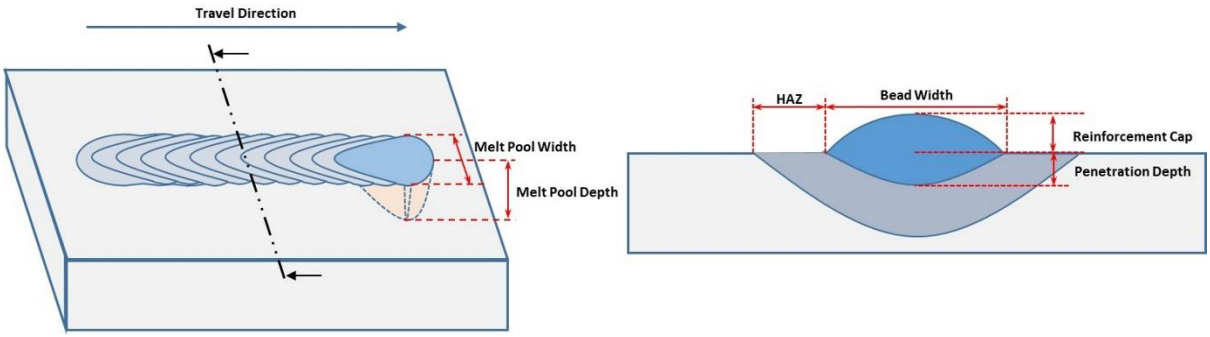

Figure 1 – Bead-on-plate welding process (left) with its corresponding cross section (right). The melt pool width corresponds to the width of the bead whereas the melt pool depth defines the penetration depth.

It is therefore required to investigate changes in the weld bead geometry utilizing the variety of current modes provided by Pulsed-GTAW. In Figure 2a a cross section of a general weld bead geometry with high penetration is presented. While this geometry is ideal for the root pass on the substrate, it is not beneficial for the built-up passes, as high penetration depth liquefies the previous passes and reduces the existing wall height by widening the melt pool. By reducing the penetration depth and increasing the reinforcement cap, more flattened beads are formed (Figure 2b). Additional increase in the reinforcement cap results in more "bumpy" beads (Figure 2c) where the height of the reinforcement exceeds the depth of penetration. Finally, by reducing the bead width while increasing the reinforcement cap a more rounded ball-shaped bead is formed (Figure 2d).

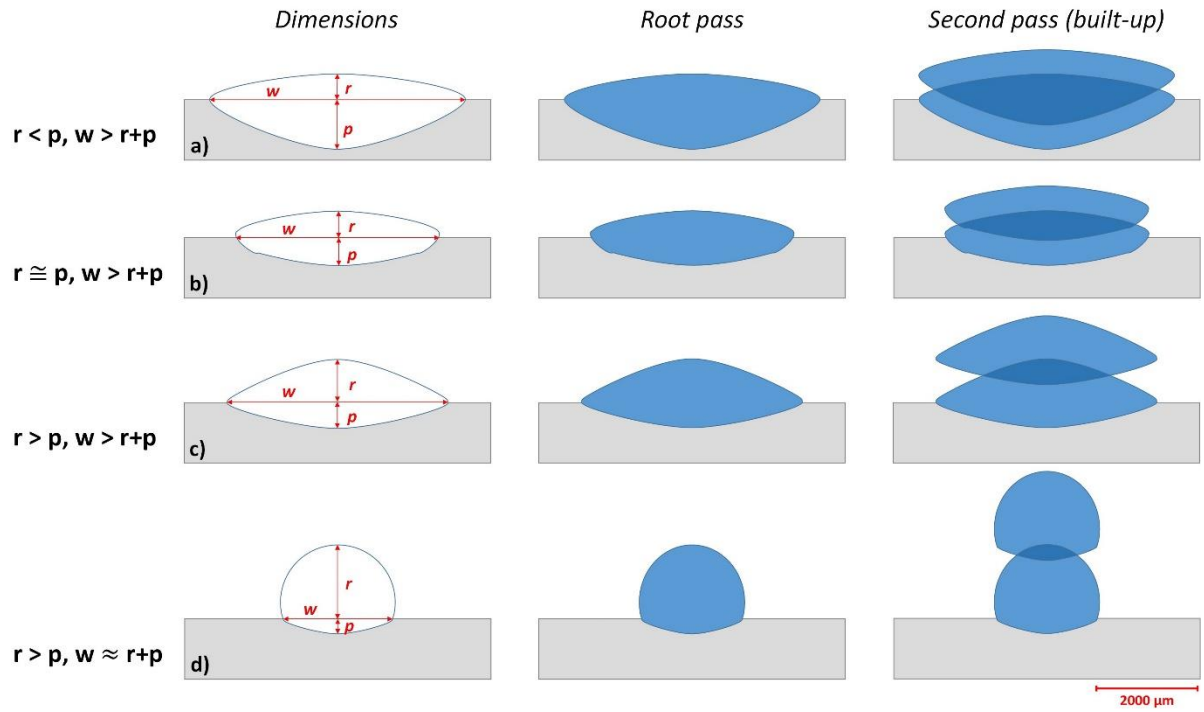

Figure 2 – Weld bead geometries characteristics for Wire Arc Additive Manufacturing (WAAM). The total bead height is defined by the reinforcement cap (r) and the penetration depth (p). Alterations in the ratios between bead height and width (w) can be utilised to form different bead geometries for root passes and secondary passes in WAAM.

Side-wall roughness should also be taken into consideration in wall build-ups, as a smoother surface closer to net shape will require less machining, while uneven surfaces will increase processing time

and material waste. Successive layer depositions should ensure overlapping bead geometries to avoid undercuts that may result in cavity formation [27].

In this paper the simultaneous control of penetration depth and bead width is attempted through alterations of pulsing modes and travel speeds in GTAW-based WAAM. The effects of these welding procedure specifications on the weld bead geometry and heat affected zone of different current modes are investigated. Direct current, low frequency thermal pulsing, high frequency pulsing and a combination of both low and high frequency pulsing (double pulse) were applied in a series of experimental designs using filler wires of both titanium and nickel-based alloys used by the aerospace industry. The aim was to extract guidelines for parameter values and current modes utilizing the aforementioned properties of pulsing, to be used in WAAM aerospace component repair.

2 Materials and methods

2.1 Experimental setup

For this study an automatic welding system composed of a Pulsed-GTAW power source with the torch mounted on an industrial robotic arm was used to deliver beads-on-plate welds. The welding power source was an IE175i Heat Management System by VBC Instrument Engineering and the robotic arm used for the control and torch manipulation was an ABB IRB 2400/16 (Figure 3). The welding process was monitored using a sensor box custom-built by the University of Sheffield, connected to a Tektronix DPO 2022B Digital Oscilloscope, offering real-time weld current and voltage data.

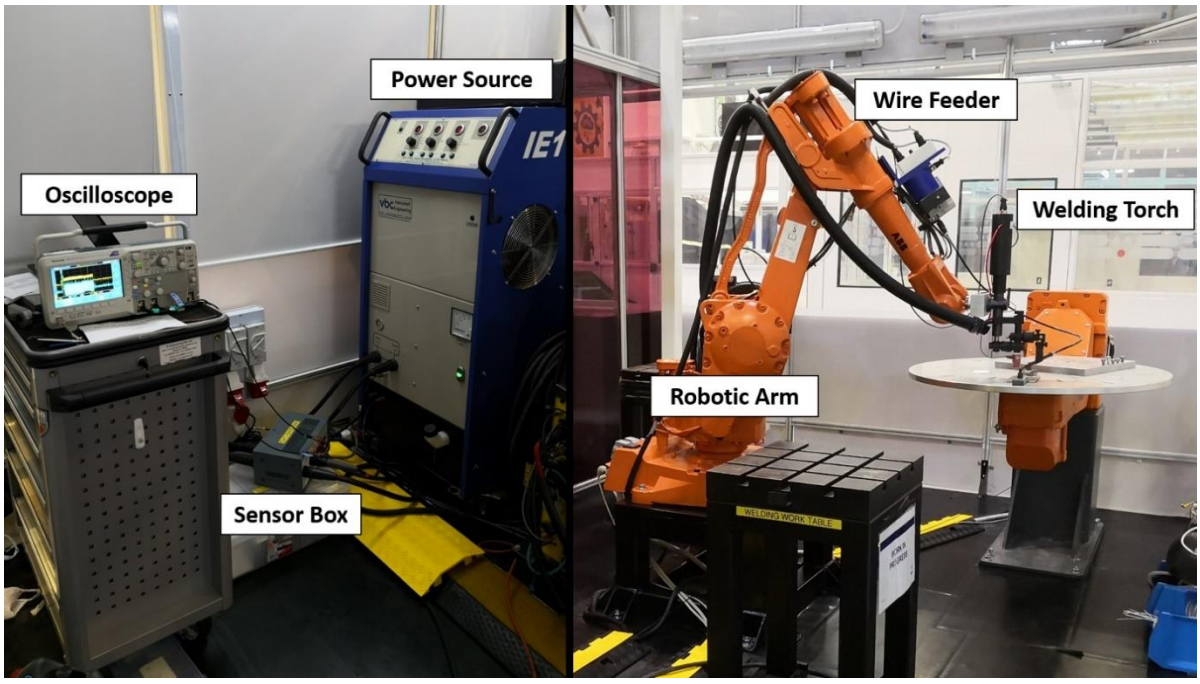

Figure 3 – The experimental setup used for GTAW-based WAAM.

2.2 Materials

Two material combinations were used in two different design of experiments which are presented below. In one set of the experiments a combination of dissimilar metals was used to highlight the geometry boundaries of the additive material on the substrate after etching, while in the other one the same material was used as both substrate and additive wire, focusing on the weld heat affected zone. On the first experimental run AMS 5832G Inconel 718 (IN718) wire (0.889 mm Ø) was used, delivering beads on Stainless Steel 316L (SS316L) 150 mm x 100 mm x 6 mm plates [28]. On the second one, AMS 4954J Ti-6Al-4V (Ti-6-4) wire (1.143 mm Ø) was used to form beads on 150 mm x 100 mm x 3 mm plates of the same material [29]. The chemical compositions of the materials are presented in Table 1 and Table 2. Localized shielding gas environment was provided in all runs using pure argon at a flow rate of 17 l/min, delivered through the welding torch cup.

Table 1 – Chemical composition of welding wire Inconel 718 (wt.%).

	Ni	Fe	Cr	Nb/Ta	Mo	Ti	Al	Co	Mn	Si	Cu	C	P	B	S
IN718	52.7	18.7	18.3	4.99	3.03	1.02	0.56	0.35	0.23	0.07	0.07	0.053	0.007	0.003	<0.002

Table 2 – Chemical composition of welding wire Ti-6-4 (wt.%).

	Ti	Al	V	C	Fe	H	N	O
Ti-6-4	Bal.	6.02	3.98	0.04	0.015	0.0125	0.02	0.13

2.3 Current modes

In order to investigate changes in weld bead geometry for additive built-up applications, five welding parameters that contribute to the outcome of the welding process were selected. Three of them, namely Main Current (I_p), Background Current (I_b) and Delta Current (I_D), are directly related to the different current modes that were investigated, while the other two were the torch travel speed and the wire feeding rate. Four different current modes were used, as presented in Figure 4. Continuous Current mode refers to direct current with no pulsing, maintaining the main value during the deposition. Slow Pulse Current mode refers to the thermal pulsing operation, where the current has the main value during the pulse duration (t_p) and the background value for the rest of the duty cycle (t_b). All the welds performed with slow pulse mode in this study had the same duty cycle δ = 50%, with both the t_p and t_b values at 0.3 s resulting in a 1.66 Hz pulsing frequency. In the InterPulse Current mode the frequency of the pulsing was set at 20,000 Hz, with the current values changing from Main to Delta every t_D = 0.025 ms. Finally, on the InterPulse Current with Slow Pulse mode, the two modes are combined providing both thermal and high frequency pulsing, resulting in current values between Main and Delta for the pulse duration (t_p), and values between Background and Delta for the

remainder duty cycle (t_b). Mean current was calculated taking into consideration the current mode used in each weld, as presented in Figure 4.

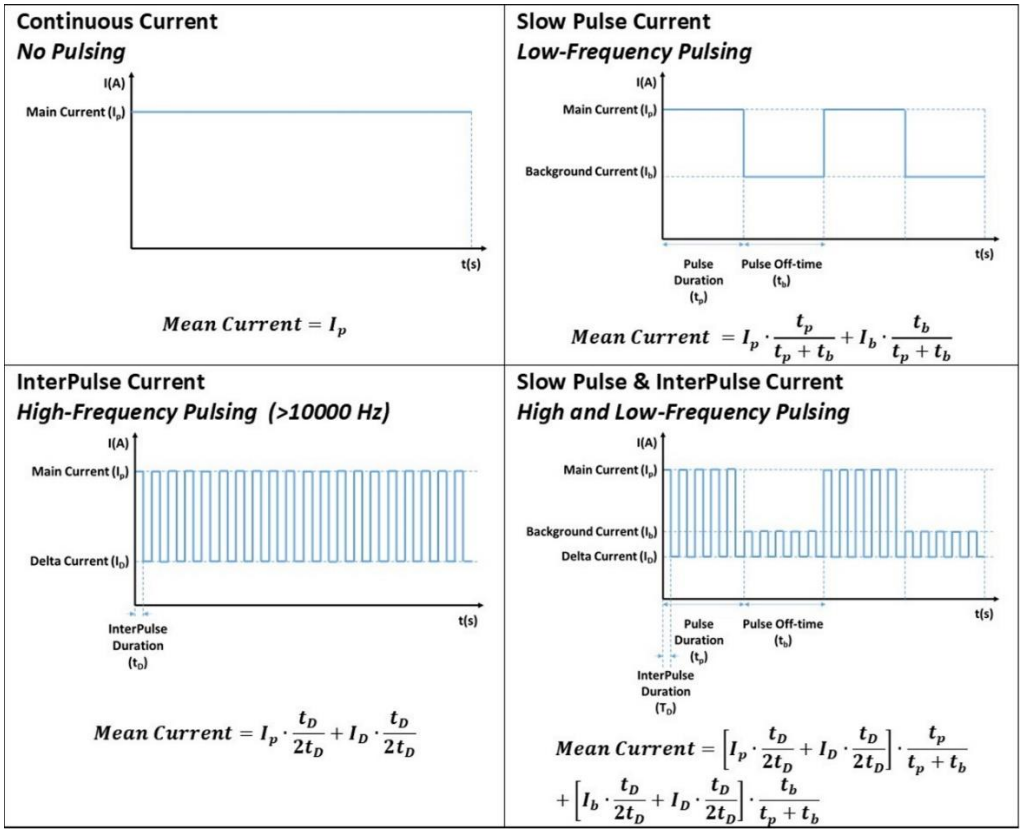

Figure 4 – Welding current modes with corresponding mean current calculations based on pulsing frequencies.

For a more clear representation in the comparison of different current modes and their effects on the weld, the heat input of each weld needed to be calculated, defined as the arc energy over the travel distance (Equation 1) [30,31]. The welding machine used is characterized as a Constant Current Power Source (CCPS), where the user presets the desired current output and the machine adjusts the voltage output based on the distance between the electrode and the workpiece. In the present work, a gauge was used to ensure the same electrode-workpiece distance in all the welds. Therefore the results related to the heat input are presented in the form of the electric charge input, defined as the charge delivered to the process per mm of travel distance (Equation 2). This form, a simpler representation, was selected to highlight the changes based on the input parameters of the operator related to the current and not on the machine-dependent (as electrode-workpiece distance was kept constant) or the process-dependent (TIG thermal efficiency) changes (Equation 3).

$$E(J/mm) = \frac{Voltage\ (V) \times Current(A) \times Process\ Thermal\ Efficiency(\%)}{Travel\ Speed(\frac{mm}{s})} \quad (1)$$

$$Electric\ Charge\ Input(\frac{C}{mm}) = \frac{Current(A)}{Travel\ Speed\ (\frac{mm}{s})} \quad (2)$$

$$E(J/mm) = Electric\ Charge\ Input(\frac{C}{mm}) \times Voltage\ (V) \times Process\ Thermal\ Efficiency(\%) \quad (3)$$

2.4 Design of experiments (DOE)

For the selection of the welding parameter values a Taguchi-inspired orthogonal array approach was followed. In the Taguchi method with a fractional factorial design the main effects and the effects of the desired interaction are allowed to be studied in a minimum number of trials [32]. By incorporating noise factors and focusing on process robustness the need for the randomization needed in the classical DOE approach is superseded. The Taguchi approach is frequently used in designing of welding experiments, in a variety of welding processes [33–35]. In the present case where the experiments implement switching between different current modes and are designed using an orthogonal array, the subsequent Taguchi analysis cannot be performed. This is because the array ceases to be orthogonal when the mean current values are calculated for a given duty cycle. In such cases a Taguchi-inspired methodology can be followed, where an initial investigation follows a fractional Taguchi design to identify contributing factors to the output and to verify a preliminary hypothesis [36]. This research stage is termed as "exploratory stage" and is followed by the "search stage" where subsequent experiments need to be run independently to establish the optimal levels of the contributing factors [36]. In this study the Taguchi approach was used with a partial factorial design as a guideline, in order to incorporate the different current modes in a single experiment. In this exploratory stage, for the five parameters selected (identified as factors in the design), three values (levels) were chosen for each experiment. The two separate experimental runs followed the L_{27}(3^5) Taguchi design (Table 3) with the values of each parameter presented on Table 4 for IN718 wire on SS316L plates and Table 5 for Ti-6-4 wire on Ti-6-4 plates.

Table 3 - DOE Partial Factorial L_{27} Orthogonal Array

Weld Number	Welding Parameters (Levels)[1]				
	Main Current	Background Current	Delta Current	Travel Speed	Wire Feed rate
1	1	1	1	1	1
2	1	1	1	1	2
3	1	1	1	1	3
4	1	2	2	2	1
5	1	2	2	2	2
6	1	2	2	2	3
7	1	3	3	3	1
8	1	3	3	3	2
9	1	3	3	3	3
10	2	1	2	3	1
11	2	1	2	3	2
12	2	1	2	3	3
13	2	2	3	1	1
14	2	2	3	1	2
15	2	2	3	1	3

16	2	3	1	2	1
17	2	3	1	2	2
18	2	3	1	2	3
19	3	1	3	2	1
20	3	1	3	2	2
21	3	1	3	2	3
22	3	2	1	3	1
23	3	2	1	3	2
24	3	2	1	3	3
25	3	3	2	1	1
26	3	3	2	1	2
27	3	3	2	1	3

[1]*For the corresponding values of each parameter see Table 4 (IN718/SS316L) and Table 5 (Ti-6-4)*

Table 4 – Welding input parameters for IN718 wire on SS316L plates.

Level	Factors				
	Main Current (A)	Background Current (A)	Delta Current (A)	Travel Speed (mm/s)	Wire Feed Speed (mm/s)
1	124	OFF	OFF	2	2
2	128	69	50	3	2.5
3	132	87	78	4	3

Table 5 – Welding input parameters for Ti-6-4 wire on Ti-6-4 plates.

Level	Factors				
	Main Current (A)	Background Current (A)	Delta Current (A)	Travel Speed (mm/s)	Wire Feed Speed (mm/s)
1	119	OFF	OFF	2	2.0
2	124	69	50	2.5	2.2
3	130	87	69	3	2.4

2.5 Optical microscopy and measurements

The welding samples were cold-mounted in epoxy resin (EpoKwick™) after being transversely sectioned using a water-cooled abrasive cutter. Gradual grounding was then performed using 180, 320, 400, 500 and 1000 Grit SiC abrasive papers sequentially. The samples were polished with 3 µm diamond suspension with the titanium samples getting an additional polishing step using colloidal silica suspension. Chemical etching was then introduced to reveal material contrasting on the Inconel/steel samples and the HAZ on the titanium samples. The reagents used for etching the titanium samples and the Inconel/steel samples were Kroll's reagent and Kalling's reagent respectively. The samples were observed and dimensions were measured using a Zeiss Axio Scope A1 microscope with AxioVision software and mosaic stitching.

3 Results and discussion

The experimental setup described was used to deliver linear bead-on-plate welds on both SS316L and Ti-6-4 plates. A total of 54 welds (27 for each material) were performed using an end effector tool path of 50 mm in length, maintaining the same electrode-workpiece distance. Representative examples for each current mode on both materials are presented in Figure 5. All the samples were prepared and chemically etched for metallography. The specimens corresponding to the welds in Figure 5 are shown in Figure 6 and Figure 7 for IN718/SS316L and Ti-6-4 respectively. Measurements were taken for determining the weld bead geometry and included weld bead width, penetration depth and weld cap reinforcement height. For the titanium samples, the penetration depth was not measured, as the additive material was the same with the substrate and the etching reagent used to reveal the HAZ did not provide clear boundaries of the bead edge. An estimation can be provided based on the changes in the microstructure, but for the purposes of this paper penetration depth was measured only on IN718/SS316L.

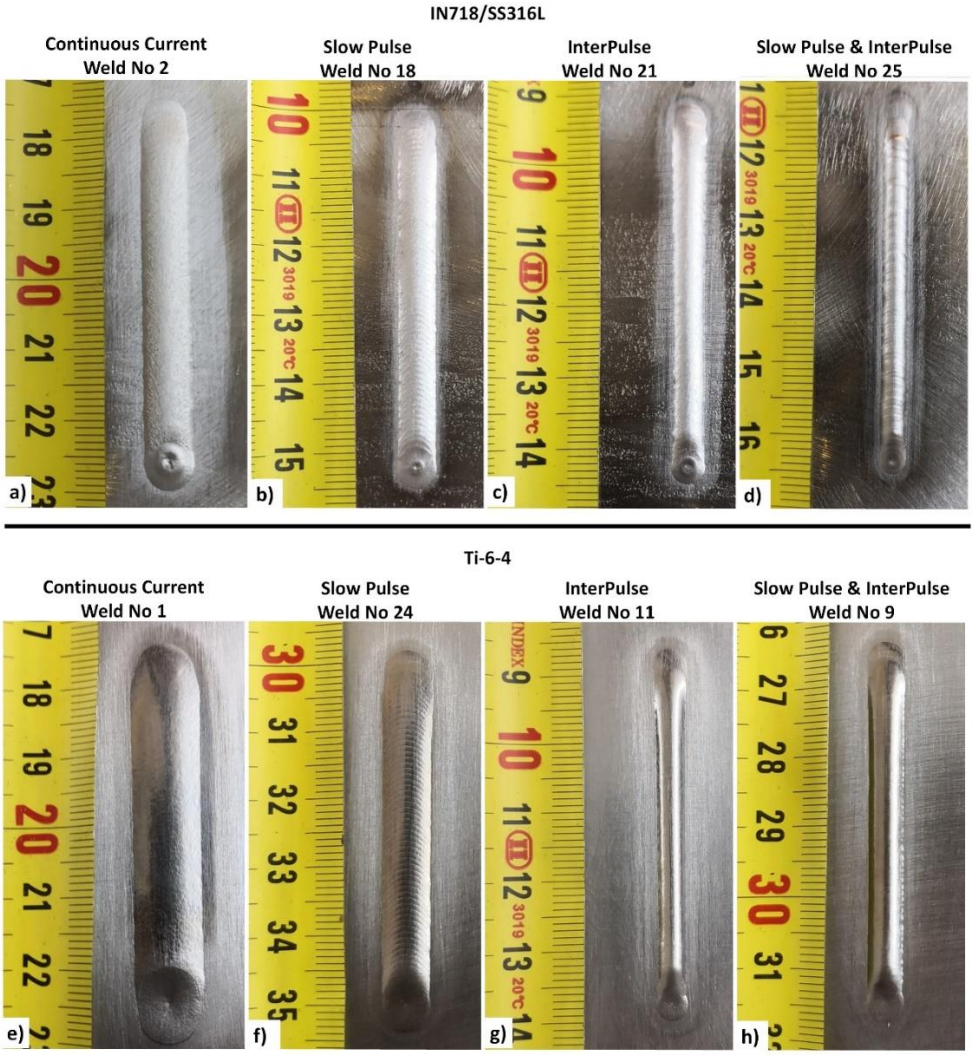

Figure 5 – Examples of linear bead-on-plate welds produced by each current mode.
Top: IN718 wire on SS316L plates (a-d); Bottom: Ti-6-4 wire on Ti-6-4 plates (e-h).

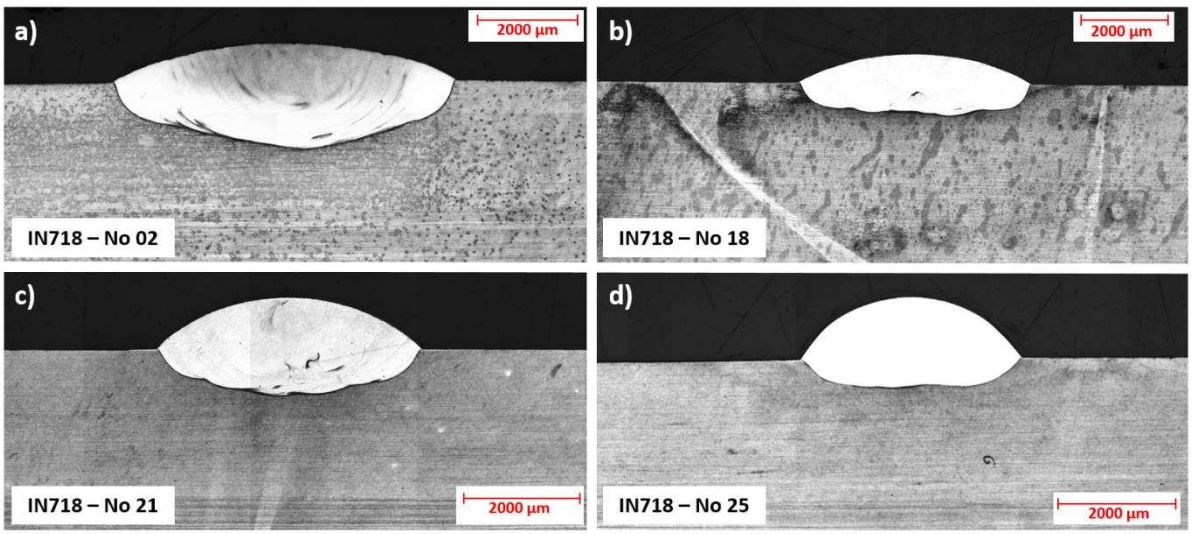

Figure 6 – Metallographic observations on etched cross sections of the IN718/SS316L linear welds from Figure 5.

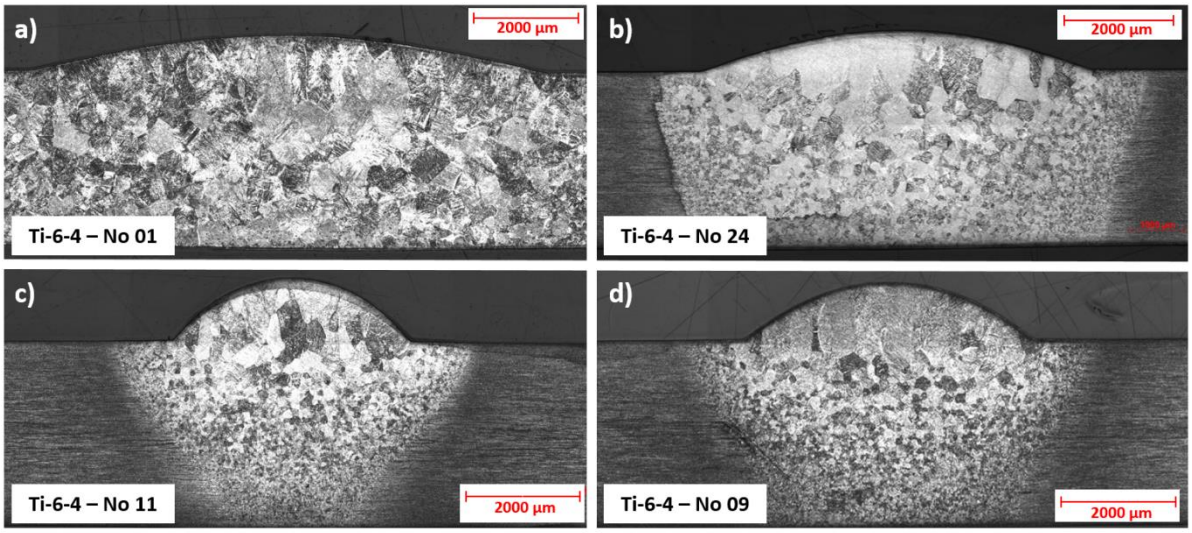

Figure 7 – Metallographic observations on etched cross sections of the Ti-6-4 linear welds from Figure 5.

3.1 Effects in geometry

From the initial post-weld visual inspections to the metallographic observations, significant changes were observed for different combinations of variables in both the weld geometries and dimensions. These changes, attributed to the variations in energy input as well as the variety of forces that contribute to the final output of the welding process, are presented.

Inconel 718

The aim of this research was to investigate the control over weld bead width simultaneously with the penetration depth. As presented in Figure 8, the experimental runs of IN718 on SS316L showed a linear correlation between the bead width and the penetration depth. Both the highest penetration depth and bead width were witnessed during the continuous current welds. The combination of the highest mean current with slow travel speed resulted in higher heat input and subsequently larger melt pool dimensions. When thermal pulsing was introduced, higher travel speeds with significantly lower mean currents reduced both the bead width and the penetration depth. Further manipulations of high frequency pulsing induced on the main current resulted in deeper penetration and wide beads for slower travel speeds and higher delta current, while showing both shallower penetration and narrow beads for higher speeds with low delta current. The combination of thermal and high-frequency pulsing, comprising the majority of the experimental runs, resulted in bead geometries grouped closer to the regression line in Figure 8. As presented in Figure 9, in the presence of high frequency pulsing, the bead width was significantly reduced compared to welds of similar heat input with only thermal pulsing. This is attributed to the arc constriction and arc root radius reduction associated with the high frequency pulsing.

Due to the fact that there were three welds for each current mode with the specific current values which differed only through the wire feed rate, the results were expected to show small groups of

three points. In comparison with the results on the bead width, the penetration depth results (Figure 10) were more disperse in grouping, as wire feed rate alterations within each group were influencing the penetration depth. In the presence of thermal pulsing, the penetration depths of similar weld runs were more concentrated than those of high frequency pulsing and continuous current.

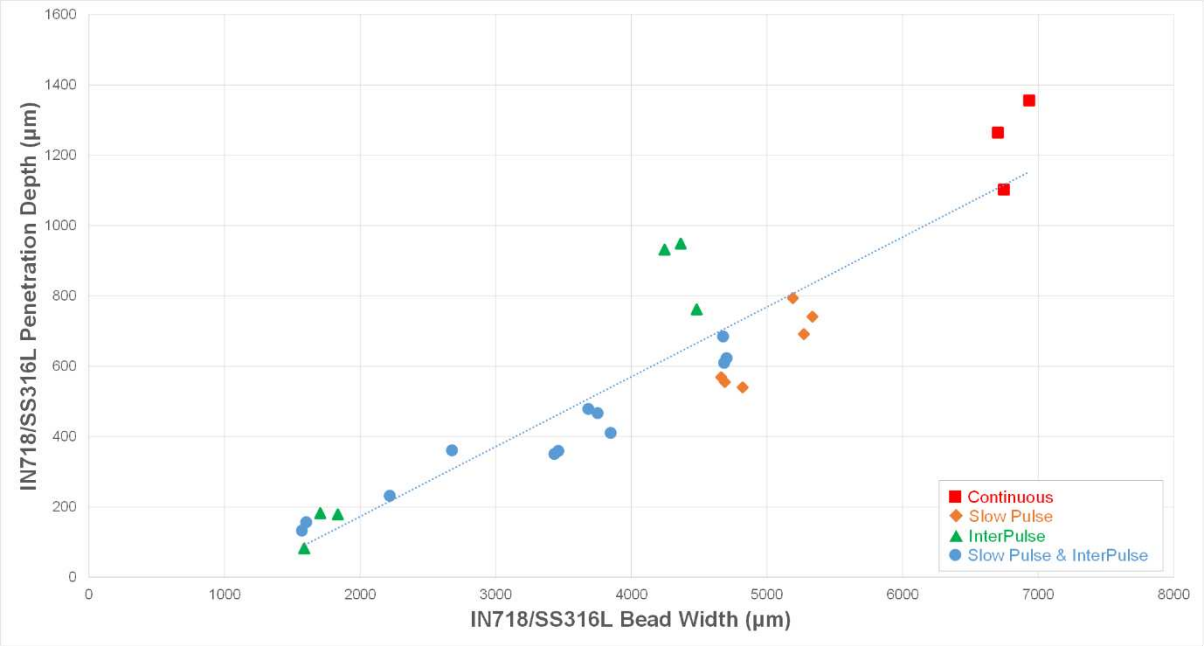

Figure 8 – Penetration depth versus bead width for IN718 on SS316L plates.

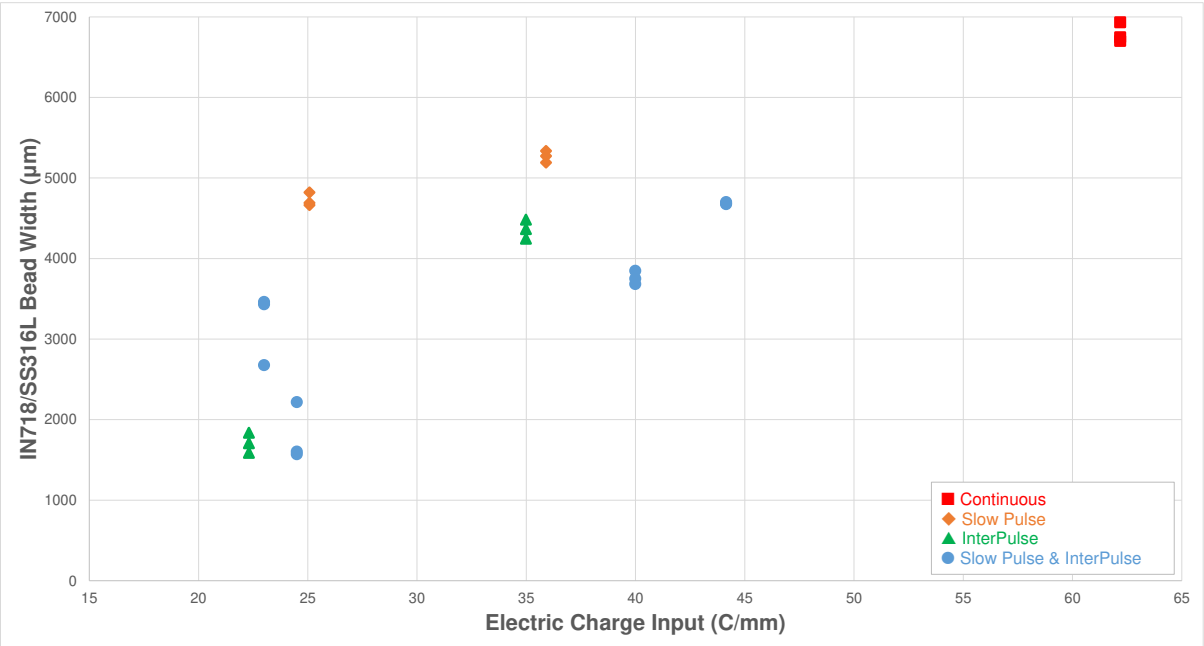

Figure 9 – Electric charge input versus bead width for IN718 on SS316L plates.

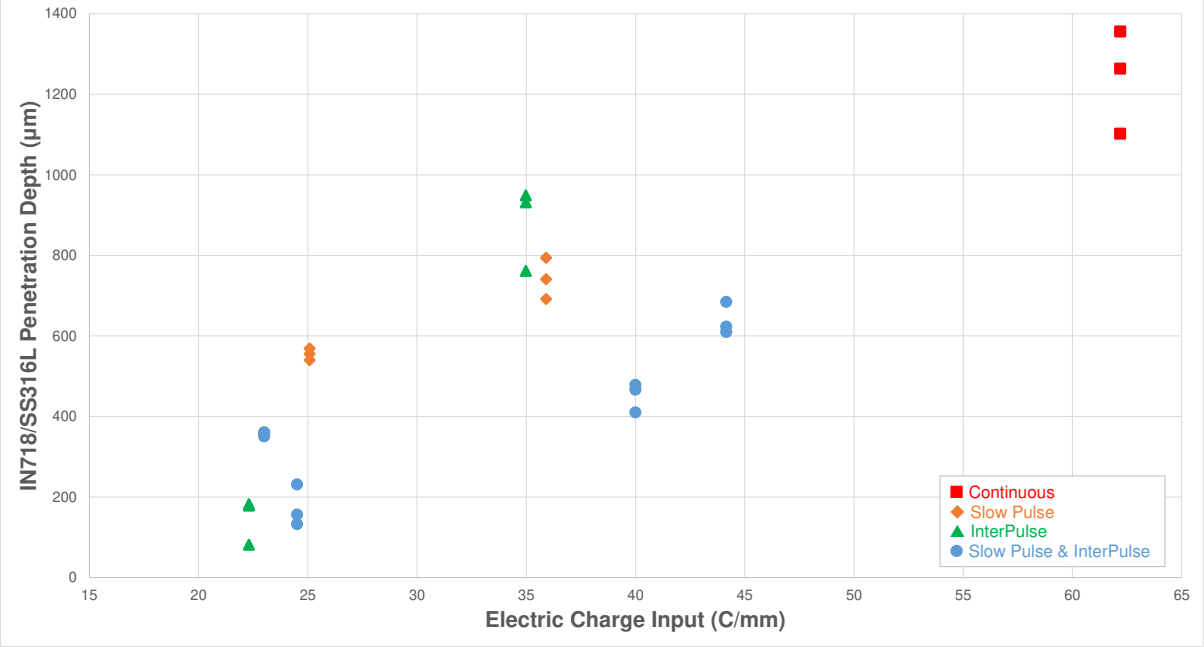

Figure 10 – Electric Charge Input results on penetration depth for IN718 on SS316L plates.

Measurements were also made on the weld reinforcement cap. In Figure 11 the resulting reinforcement to bead width ratio is presented. The more flattened beads (wide beads with short reinforcement cap) were obtained in the absence of delta current. Due to the arc constriction induced by the high frequency pulsing, narrowing of the bead width subsequently increased the reinforcement cap, creating more rounded beads with higher height-to-width ratios. Travel speed alterations and the combination of both thermal and high frequency pulsing allowed the formation of beads with a variety of height-to-width ratios.

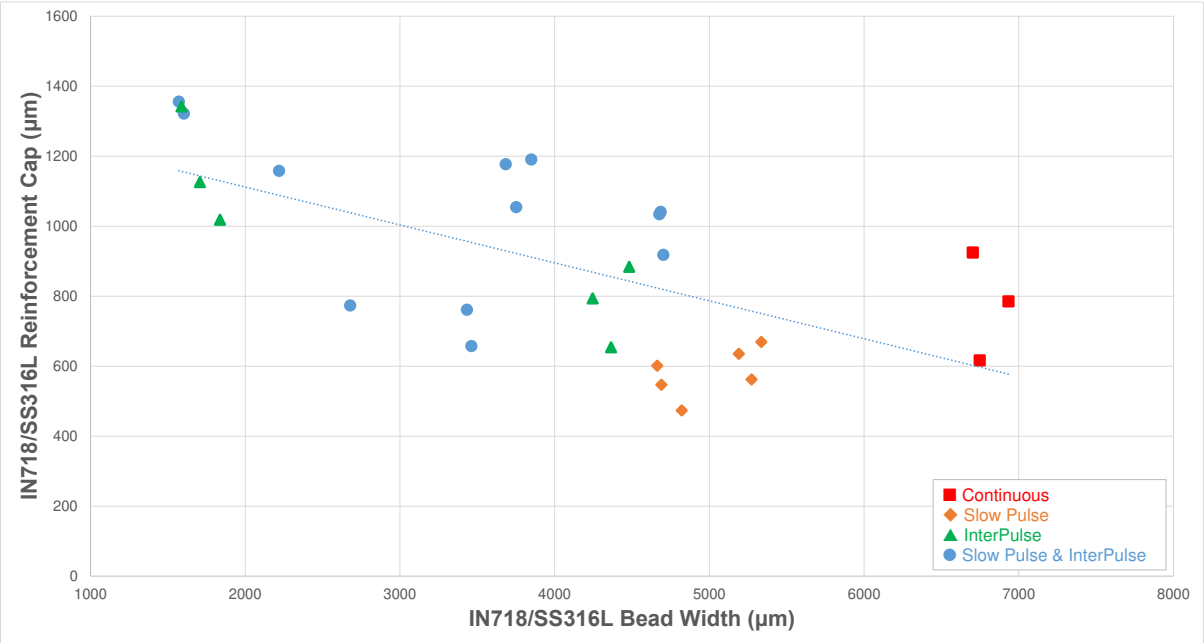

Figure 11 – Reinforcement cap and bead width for IN718 on SS316L plates.

In Figure 12 the effects on the total weld bead height – taking into consideration both the penetration depth and the reinforcement cap – are presented. The lowest total height to penetration depth ratios resulted from welds utilising continuous current (Figure 12a) while significantly higher ratios were obtained in welds with high frequency pulsing (Figure 12b). Flattened elongated welds with about 1:1 penetration depth to reinforcement cap ratio were witnessed on thermal pulsing welds (Figure 12c). On low heat inputs (Figure 13) the high frequency pulsing provided manyfold increases in the total-height-to-penetration depth ratio. As the heat input increases, when only one form of pulsing is utilised, the accumulated heat results in high penetration, subsequently resulting in lower ratios. When both thermal and high frequency pulsing are utilised, even on higher heat inputs the weld bead geometries maintain higher total-height-to-penetration ratios.

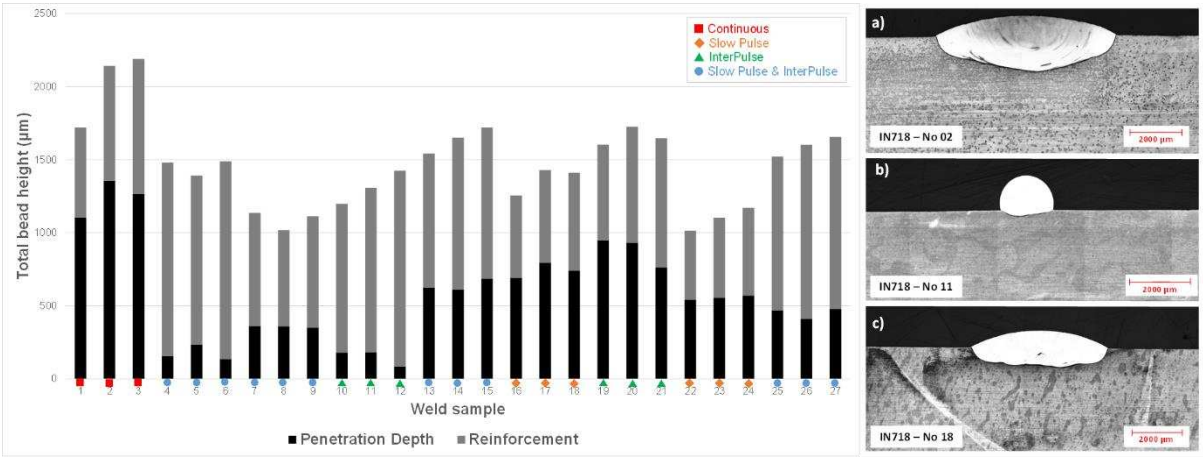

Figure 12 – Left: Total weld bead height as a combination of the penetration depth and the reinforcement cap for all the IN718 beads on SS316L plates. Right: Representative examples of bead geometries. Deep welds high penetration depth (a), high reinforcement cap with low penetration depth (b) and welds where the total height is evenly distributed between penetration depth and reinforcement cap (c).

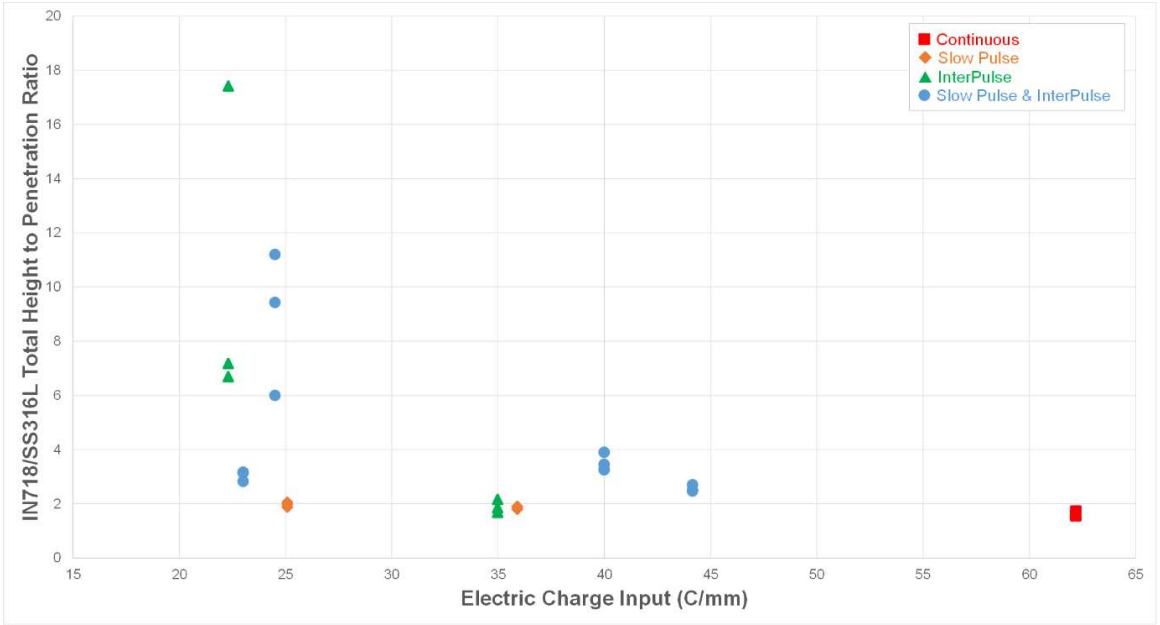

Figure 13 – Electric charge input versus total height-to-penetration ratio for IN718 on SS316L plates.

Titanium Ti-6-4

The effects on the weld bead geometry for the titanium samples were in general similar to those of Inconel. As presented in Figure 14, the resulting Ti-6-4 bead width changes in the experimental runs showed a response similar with IN718/SS316L. With the experiments following the same orthogonal array design, thermal pulsing and high frequency pulsing of similar heat input caused the same variations in the geometries. Changes to the bead size distribution in comparison with IN718/SS316L are mainly attributed to the different input parameter values between the two designs of experiments.

Similar results were also witness on the reinforcement cap measurements. The reinforcement to bead width ratio on Ti-6-4 followed the same type of distribution as the IN718/SS316L, with a slightly different trendline (Figure 15). The more rounded beads with high height-to-width ratios were again witnessed in the presence of delta current while flattened beads were obtained in the absence of delta current, highlighting similar behaviour for both materials.

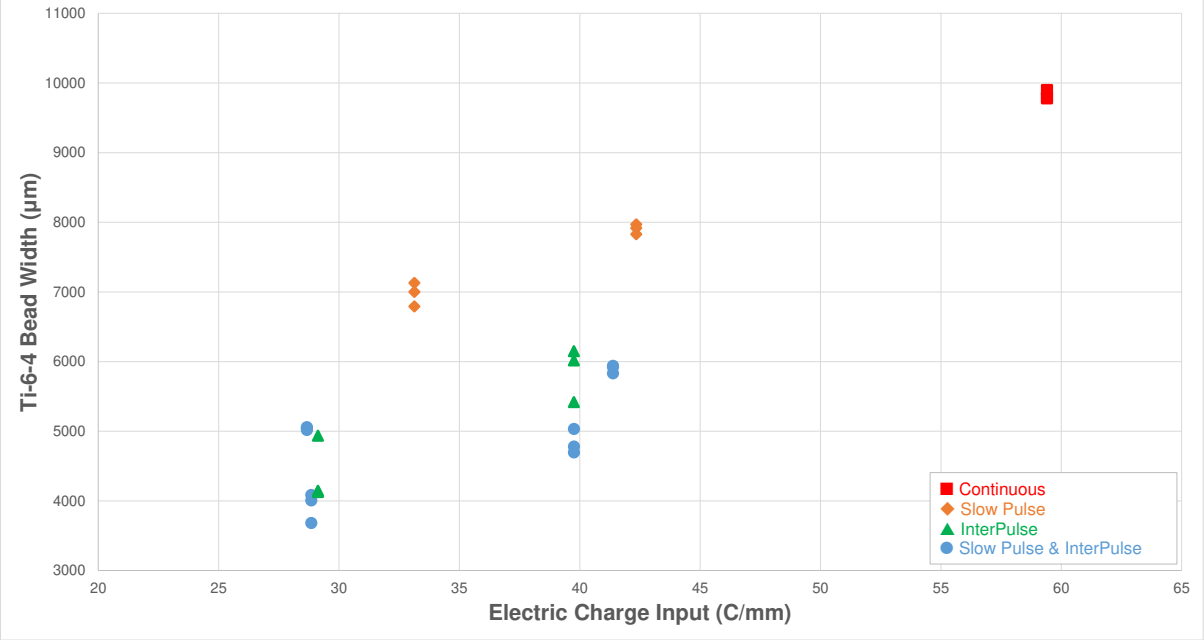

Figure 14 – Electric charge input versus bead width for Ti-6-4.

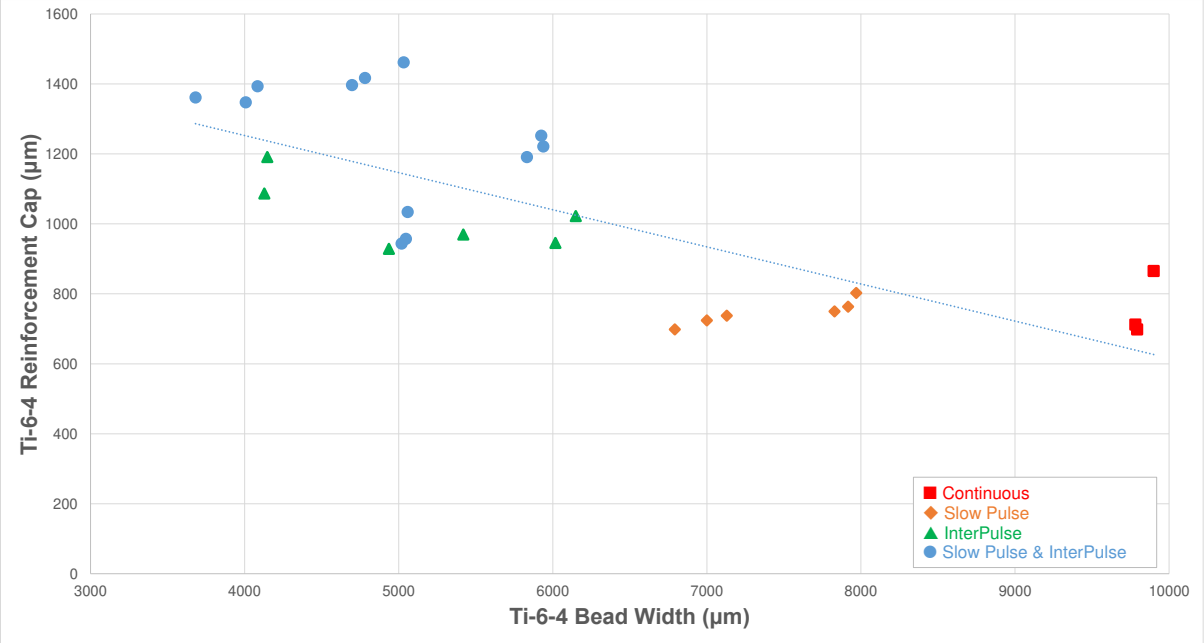

Figure 15 – Reinforcement cap and bead width for Ti-6-4.

3.2 Effects in heat affected zone

The titanium samples were etched in order to reveal the microstructure changes post-weld, and highlight the heat affected zone in each weld. The HAZ was measured only in width, as the heat affected regions were detected throughout the whole thickness of the material. To calculate the correct HAZ width on the titanium samples, measurements were taken from the center of the bead width to the edge of the affected zone following a subtraction of the actual bead width size (Figure 16).

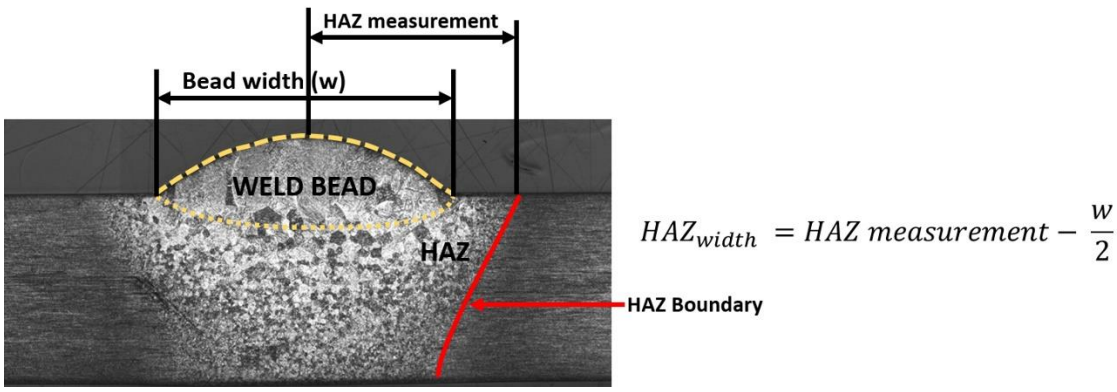

Figure 16 – HAZ measurements.

The HAZ width as a function of the heat input, shown in Figure 17, reveals a blend of HAZ width sizes through different heat inputs and current modes, with no clear indication of correlated changes. When focusing however on the total cross-section of the HAZ and not only on the surface width measurement, there is a clear change in the shape and directionality of the high heat zone in the material. As presented on Figure 18, five main variations in shape were detected. The arc constriction

and higher charge density induced by the high frequency pulsing allowed directionality in the heat distribution, resulting in an arrow-shaped heat affected region. The effects are more obvious in welds of similar heat input (Figure 19) utilizing different current modes. On weld No 17 thermal pulsing resulted in a trapezoid-shaped heat affected region, whereas on weld No 15, the combination of thermal pulsing with InterPulse allowed a heat affected region with a narrower bottom and more notable sigmoid boundary lines.

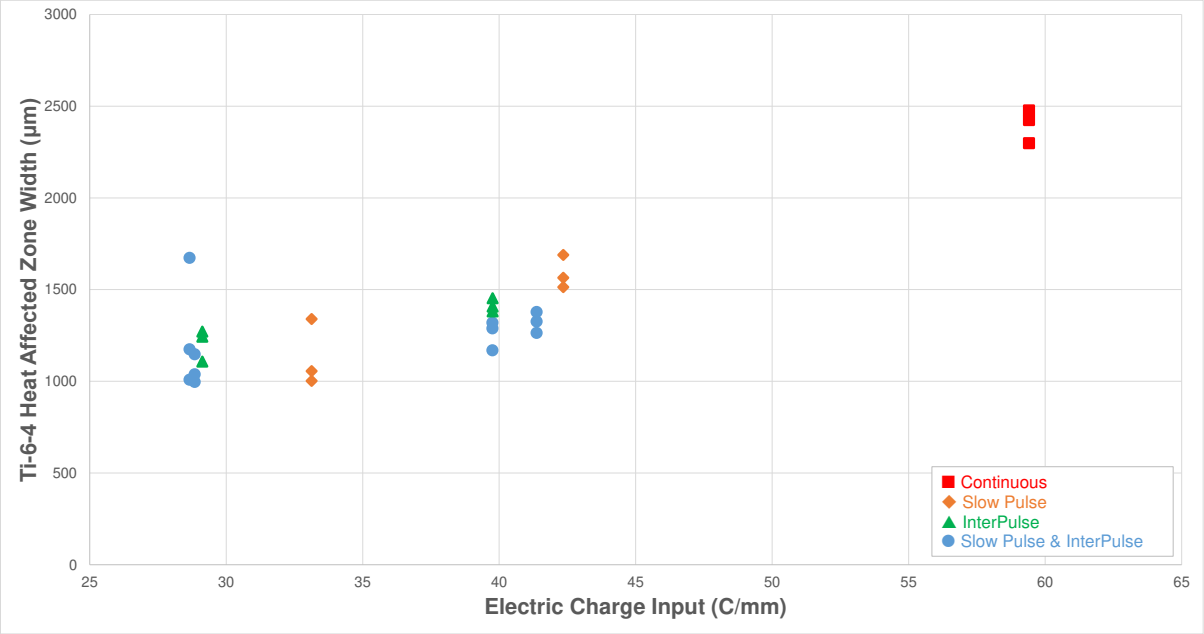

Figure 17 – Heat affected zone width results on Ti-6-4.

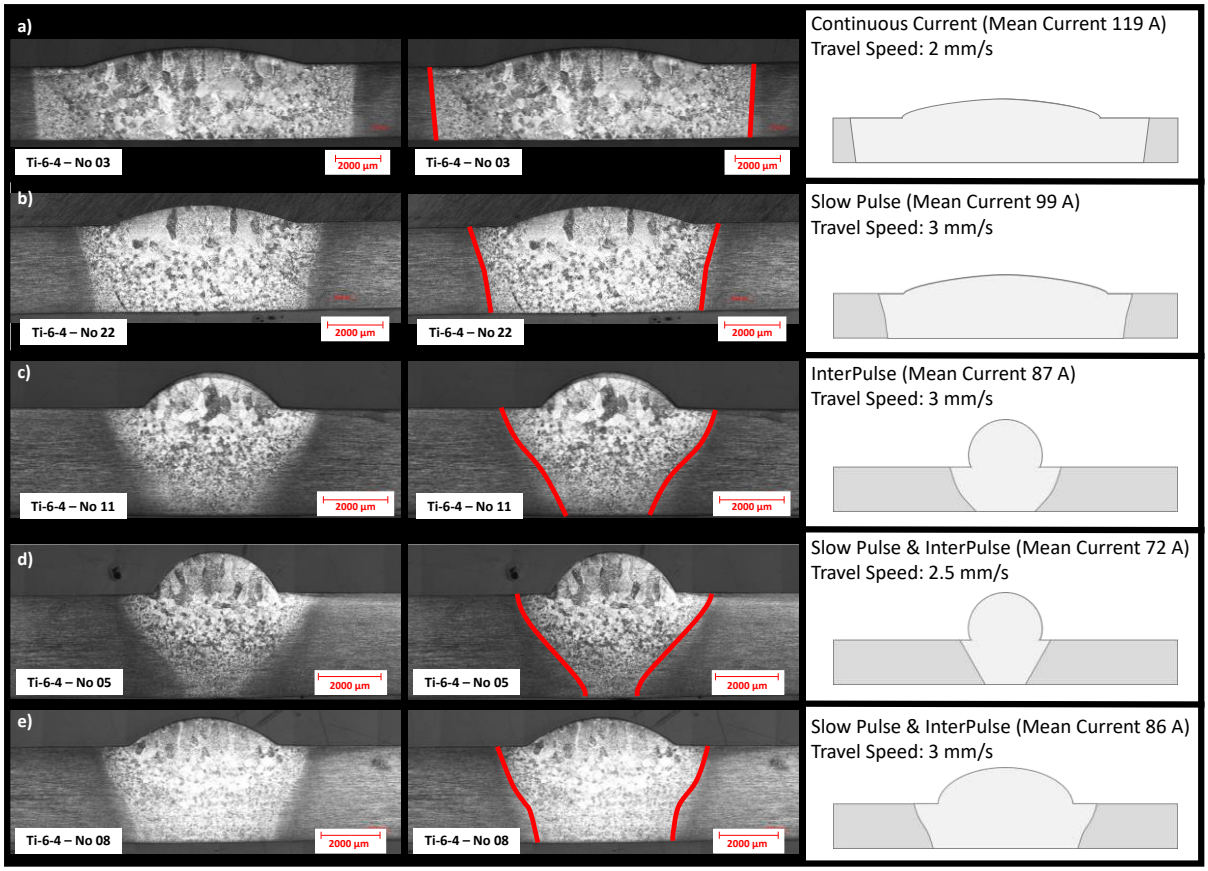

Figure 18 – Heat affected region shape on different current modes. Changes in the directionality of the heat region resulted from introducing pulsed currents and simultaneously altering the travel speeds.

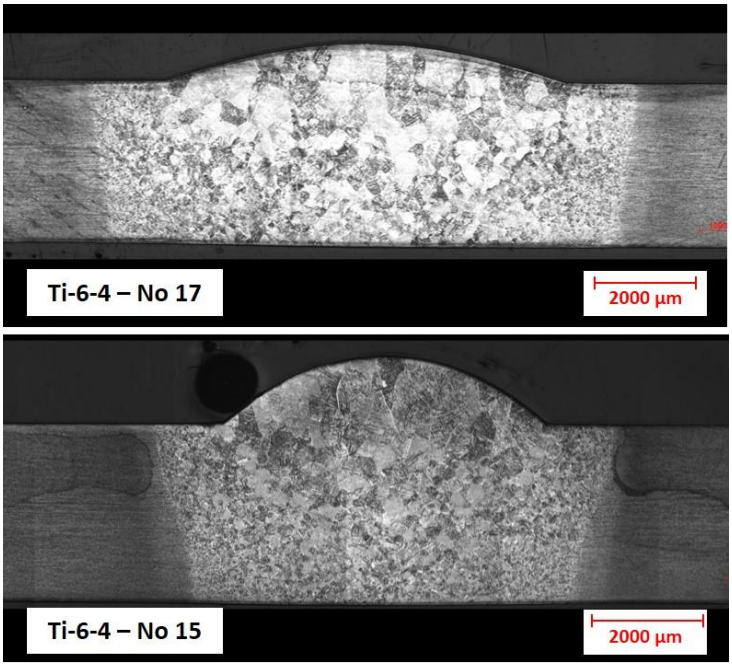

Figure 19 - Heat affected zone shape changes on weld with similar heat input (top: thermal pulsing, bottom thermal pulsing with InterPulse)

3.3 Current mode evaluation

In WAAM and AM in general the ideal weld bead would have been one that combines sufficient penetration, tall cap reinforcement and lower heat input for narrowing the HAZ and lowering residual stresses. The weld bead width would be selected depending on the application, however narrower beads result in higher printing resolution, allowing more manufacturing dexterity and builds closer to the net-shape than with wider beads. Therefore high height-to-width ratio is preferred.

From the measurements presented, the tallest cap reinforcement and the highest height-to-width ratio was achieved by the ball-shaped beads utilizing low InterPulse currents and high travel speeds. These welds however experienced the lowest penetration depth, and would likely result in failures, jeopardizing structural integrity. Both high height-to-width ratio and tall weld cap reinforcement, while at the same time achieving moderate penetration depth was witnessed in welds No 25, No 26 and No 27. To fabricate these welds, that resulted in the cardioid-shaped beads and the sigmoid HAZ, the combination of high and low frequency pulsing was used with low travel speed.

When thermal pulsing was used without high frequency pulsing, high penetration and elongated beads were achieved, but with minimal cap reinforcement. By contrast, when InterPulse current was used without thermal pulsing the beads showed tall cap reinforcement with high height-to-width ratio.

When high and low frequency pulsing are used simultaneously, the mean current value can be reduced significantly compared to continuous current modes. This allows lower heat input and subsequently a reduction in the heat affected area, without compromising the weld specification. It is highlighted that welds No 25, No 26 and No 27 were fabricated using the second lowest mean current values of the whole DOE.

With regards to the process performance in relation with the material used, comparable bead geometries were witnessed in both the experimental runs for the same current modes. However, in order to get beads with desired dimensions on a specific material, individual Taguchi experiments with a single current mode should be performed for every material. Therefore the subsequent Taguchi analysis will be enabled and provide the process optimization be means of variance analysis.

3.4 Application of the results in WAAM

Implementations of the findings of this research was carried out in an initial step for the repair and re-manufacturing of aerospace components. Based on the aforementioned analysis, for the specific set of parameters, the current-mode of choice for the built-up of additive material via WAAM would be the combination of both high and low frequency pulsing. However, for achieving highest penetration

on the substrate during the root pass and thus enabling a more stable structure to be built, the combination of a high-energy continuous current root pass followed by a series of built-up passes with high and low frequency current modulation was selected for the process. Using the welding parameters of Weld 3 and Weld 27, a series of linear welds were produced with Ti-6-4 successively, as presented in Figure 20. The high penetration of the root pass allowed the formation of a wide bead, eliminating the effect of undercut and preventing the formation of concavities. Subsequently, the combination of both high and low frequency pulsing allowed the formation of narrower beads with taller reinforcement caps and shallower penetration, resulting in beneficial geometries for built-up. Attributed to the dexterity on complementary shape-matching of the successive layers, no lack of fusion was witnessed, allowing smoother side-wall surfaces to be formed, reducing the uneven side-wall roughness that otherwise occurs. Additional work is required to optimize the bead geometry for WAAM applications that will allow a greater number of successive layers and the opportunity to evaluate the pulsing effects in taller built-ups.

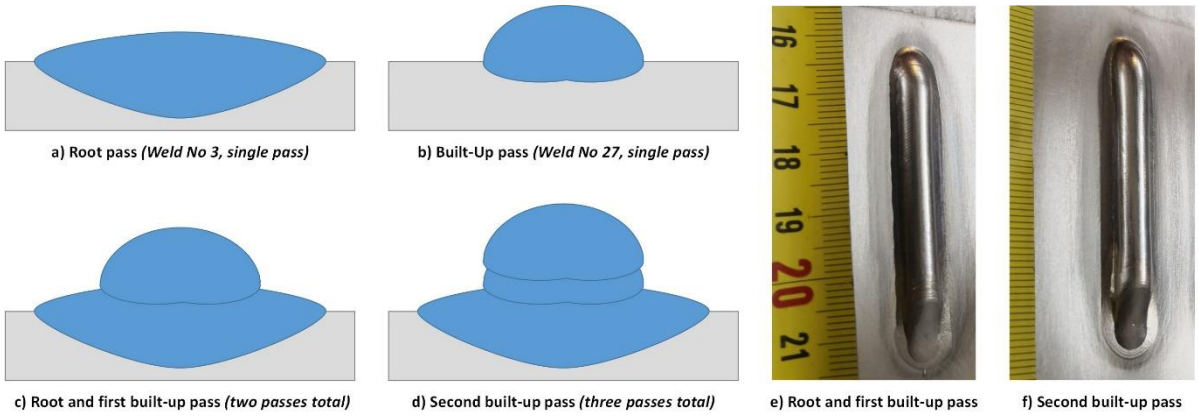

Figure 20 – Combination of continuous current root pass with pulsed-current build-up passes in WAAM (Ti-6-4).

4 Conclusions

In this paper the ability of a single Pulsed-GTAW setup to create a variety of bead geometries using high and low frequency pulsing was investigated on Inconel-718 and Ti-6-4 materials. It is concluded that depending on the geometries desired for each specific application, Pulsed-GTAW can produce a variety of bead geometries by utilizing the beneficial effects of a pulsing current power source. The combination of both high and low frequency pulsing with manipulations on travel speed coupled with wire feeding rate alterations can be used to control weld bead characteristics like reinforcement cap height and bead width, as well as penetration depth. The lower heat input and arc constriction induced by the high-frequency pulsing can also be utilized to reduce the heat affected region by narrowing the root base of the heat affected zone.

The investigated process allowed the formation of both high penetration/wide bead welds suitable for root passes, as well as low penetration/narrow beads ideal for built-up in secondary passes, all in the same experimental setup that can be utilized for WAAM. The process demonstrated comparable results in both Inconel-718 and Ti-6-4 experimental runs that followed similar Taguchi-inspired orthogonal array designs. Future work is required in order to optimize the output of each current mode in specific applications and to validate the process effects in additive manufacturing.

Acknowledgements

The research was performed under an industry-academia collaboration between the Physics and Astronomy Department of the University of Sheffield in United Kingdom and the A*STAR's Advanced Remanufacturing and Technology Centre (ARTC) in Singapore, under the A*STAR Research Attachment Programme (ARAP).

Declaration of interest

The authors declare that they have no known competing financial interests or personal relationships that could have appeared to influence the work reported in this paper.

References

[1] Lu QY, Wong CH. Additive manufacturing process monitoring and control by non-destructive testing techniques: challenges and in-process monitoring. Virtual Phys Prototyp 2018;13:39–48. https://doi.org/10.1080/17452759.2017.1351201.

[2] Everton SK, Hirsch M, Stavroulakis PI, Leach RK, Clare AT. Review of in-situ process monitoring and in-situ metrology for metal additive manufacturing. Mater Des 2016;95:431–45. https://doi.org/10.1016/j.matdes.2016.01.099.

[3] Szost BA, Terzi S, Martina F, Boisselier D, Prytuliak A, Pirling T, et al. A comparative study of additive manufacturing techniques: Residual stress and microstructural analysis of CLAD and WAAM printed Ti-6Al-4V components. Mater Des 2016;89:559–67. https://doi.org/10.1016/j.matdes.2015.09.115.

[4] Van D, Dinda GP, Park J, Mazumder J, Lee SH. Enhancing hardness of Inconel 718 deposits using the aging effects of cold metal transfer-based additive manufacturing. Mater Sci Eng A 2020;776:139005. https://doi.org/10.1016/j.msea.2020.139005.

[5] Yusuf SM, Cutler S, Gao N. Review: The impact of metal additive manufacturing on the aerospace industry. Metals (Basel) 2019;9. https://doi.org/10.3390/met9121286.

[6] Jin W, Zhang C, Jin S, Tian Y, Wellmann D, Liu W. Wire Arc Additive Manufacturing of Stainless Steels: A Review. Appl Sci 2020;10:1563. https://doi.org/10.3390/app10051563.

[7] Cunningham CR, Flynn JM, Shokrani A, Dhokia V, Newman ST. Invited review article: Strategies and processes for high quality wire arc additive manufacturing. Addit Manuf 2018;22:672–86. https://doi.org/10.1016/j.addma.2018.06.020.

[8] Li F, Chen S, Wu Z, Yan Z. Adaptive process control of wire and arc additive manufacturing for

fabricating complex-shaped components. Int J Adv Manuf Technol 2018;96:871–9. https://doi.org/10.1007/s00170-018-1590-0.

[9] Wu B, Pan Z, Ding D, Cuiuri D, Li H, Xu J, et al. A review of the wire arc additive manufacturing of metals: properties, defects and quality improvement. J Manuf Process 2018;35:127–39. https://doi.org/10.1016/j.jmapro.2018.08.001.

[10] Xu F, Dhokia V, Colegrove P, McAndrew A, Williams S, Henstridge A, et al. Realisation of a multi-sensor framework for process monitoring of the wire arc additive manufacturing in producing Ti-6Al-4V parts. Int J Comput Integr Manuf 2018;31:785–98. https://doi.org/10.1080/0951192X.2018.1466395.

[11] Zhang YM, Chen Y, Li P, Male AT. Weld deposition-based rapid prototyping: A preliminary study. J Mater Process Technol 2003;135:347–57. https://doi.org/10.1016/S0924-0136(02)00867-1.

[12] Selvi S, Vishvaksenan A, Rajasekar E. Cold metal transfer (CMT) technology - An overview. Def Technol 2018;14:28–44. https://doi.org/10.1016/j.dt.2017.08.002.

[13] Williams SW, Martina F, Addison AC, Ding J, Pardal G, Colegrove P. Wire + Arc additive manufacturing. Mater Sci Technol (United Kingdom) 2016;32:641–7. https://doi.org/10.1179/1743284715Y.0000000073.

[14] Baghel PK, Nagesh DS. Pulse TIG welding: Process, Automation and Control. J Weld Join 2017;35:43–8. https://doi.org/10.5781/jwj.2017.35.1.43.

[15] Ghosh PK. Pulse Current Gas Metal Arc Welding. Springer Singapore; 2017. https://doi.org/10.1007/978-981-10-3557-9_10.

[16] Norrish J. Advanced Welding Processes. Woodhead Publishing Limited; 2006. https://doi.org/10.1533/9781845691707.

[17] Lucas W. TIG and Plasma welding. 1990. https://doi.org/10.1533/9780857093264.

[18] A SJ. Pulsed Arc Welding. Abington Publishing; 1990.

[19] Wu Q, Ma Z, Chen G, Liu C, Ma D, Ma S. Obtaining fine microstructure and unsupported overhangs by low heat input pulse arc additive manufacturing. J Manuf Process 2017;27:198–206. https://doi.org/10.1016/j.jmapro.2017.05.004.

[20] Ahmed N. Direct metal fabrication in rapid prototyping: A review. J Manuf Process 2019;42:167–91. https://doi.org/10.1016/j.jmapro.2019.05.001.

[21] Pal K, Pal SK. Effect of pulse parameters on weld quality in pulsed gas metal arc welding: A review. J Mater Eng Perform 2011;20:918–31. https://doi.org/10.1007/s11665-010-9717-y.

[22] Qi BJ, Yang MX, Cong BQ, Liu FJ. The effect of arc behavior on weld geometry by high-frequency pulse GTAW process with 0Cr18Ni9Ti stainless steel. Int J Adv Manuf Technol 2013;66:1545–53. https://doi.org/10.1007/s00170-012-4438-z.

[23] Yang M, Qi B, Cong B, Liu F, Yang Z, Chu PK. Study on electromagnetic force in Arc plasma with UHFP-GTAW of Ti-6Al-4V. IEEE Trans Plasma Sci 2013;41:2561–8. https://doi.org/10.1109/TPS.2013.2274810.

[24] Yang M, Li L, Qi B, Zheng H. Arc force and shapes with high-frequency pulsed-arc welding. Sci Technol Weld Join 2017;22:580–6. https://doi.org/10.1080/13621718.2016.1277625.

[25] Cook EG, Eassa HEDEH. The Effect of High-Frequency Pulsing of a Welding Arc. IEEE Trans Ind

Appl 1985;IA-21:1294–9. https://doi.org/10.1109/TIA.1985.349557.

[26] Yang M, Zheng H, Li L. Arc shape characteristics with ultra-high-frequency pulsed arc welding. Appl Sci 2017;7. https://doi.org/10.3390/app7010045.

[27] Ding D, Pan Z, Cuiuri D, Li H. A multi-bead overlapping model for robotic wire and arc additive manufacturing (WAAM). Robot Comput Integr Manuf 2015;31:101–10. https://doi.org/10.1016/j.rcim.2014.08.008.

[28] SAE International. AMS5832G: AEROSPACE MATERIAL SPECIFICATION - Nickel Alloy, Corrosion and Heat Resistant, Welding Wire 52.5Ni - 19Cr - 3.0Mo - 5.1Cb(Nb) - 0.90Ti - 0.50Al - 18Fe Consumable Electrode or Vacuum Induction Melted 2020.

[29] SAE International. AMS4954J: AEROSPACE MATERIAL SPECIFICATION - Titanium Alloy, Welding Wire 6Al - 4V 2009.

[30] Ogundimu EO, Akinlabi ET, Erinosho MF. An Experimental Study on the Effect of Heat Input on the Weld Efficiency of TIG-MIG Hybrid welding of Type 304 Austenitic Stainless Steel. J Phys Conf Ser 2019;1378. https://doi.org/10.1088/1742-6596/1378/2/022075.

[31] Ruiz-Vela JI, Montes-Rodríguez JJ, Rodríguez-Morales E, Toscano-Giles JA. Effect of cold metal transfer and gas tungsten arc welding processes on the metallurgical and mechanical properties of Inconel® 625 weldings. Weld World 2019;63:459–79. https://doi.org/10.1007/s40194-018-0661-z.

[32] Antony J. Design of Experiments for Engineers and Scientists. Elsevier Science and Technology Books; 2003. https://doi.org/10.1016/B978-0-7506-4709-0.X5000-5.

[33] Schneider C, Lisboa C, Silva R, Lermen R. Optimizing the Parameters of TIG-MIG/MAG Hybrid Welding on the Geometry of Bead Welding Using the Taguchi Method. J Manuf Mater Process 2017;1:14. https://doi.org/10.3390/jmmp1020014.

[34] Guo N, Cheng Q, Fu Y, Du Y, Zhang X, Feng J. Investigation on the mass transfer control, process stability and welding quality during underwater pulse current FCAW for Q235. J Manuf Process 2019;46:317–27. https://doi.org/10.1016/j.jmapro.2019.08.022.

[35] Prajapati V, Dinbandhu, Vora JJ, Das S, Abhishek K. Study of parametric influence and welding performance optimization during regulated metal deposition (RMD™) using grey integrated with fuzzy taguchi approach. J Manuf Process 2020;54:286–300. https://doi.org/10.1016/j.jmapro.2020.03.017.

[36] Trietsch D. A Proposal to Apply Taguchi-Inspired Methods to the Reduction of Machining Variance. Dept Adm Sci Nav Postgrad Sch 1992;NPS-AS-92-:1–30.